

**Vibrationally mediated photolysis dynamics of H<sub>2</sub>O in the  $\nu$  OH =3 manifold: Far off resonance photodissociation cross sections and OH product state distributions**

Ondrej Votava, David F. Plusquellic, and David J. Nesbitt

Citation: *The Journal of Chemical Physics* **110**, 8564 (1999); doi: 10.1063/1.478764

View online: <http://dx.doi.org/10.1063/1.478764>

View Table of Contents: <http://scitation.aip.org/content/aip/journal/jcp/110/17?ver=pdfcov>

Published by the [AIP Publishing](#)

---

**Articles you may be interested in**

[Photodissociation of N<sub>2</sub>O: Energy partitioning](#)

*J. Chem. Phys.* **135**, 024311 (2011); 10.1063/1.3602324

[Ab initio potential energy surfaces, total absorption cross sections, and product quantum state distributions for the low-lying electronic states of N<sub>2</sub>O](#)

*J. Chem. Phys.* **122**, 054305 (2005); 10.1063/1.1830436

[Dissociation dynamics of thiolactic acid at 193 nm: Detection of the nascent OH product by laser-induced fluorescence](#)

*J. Chem. Phys.* **120**, 6964 (2004); 10.1063/1.1667878

[Spectrum and vibrational predissociation of the HF dimer. II. Photodissociation cross sections and product state distributions](#)

*J. Chem. Phys.* **119**, 286 (2003); 10.1063/1.1577112

[Photodissociation dynamics of acetylacetone: The OH product state distribution](#)

*J. Chem. Phys.* **110**, 11850 (1999); 10.1063/1.479126

---



# Vibrationally mediated photolysis dynamics of H<sub>2</sub>O in the $\nu_{\text{OH}}=3$ manifold: Far off resonance photodissociation cross sections and OH product state distributions

Ondrej Votava, David F. Plusquellic,<sup>a)</sup> and David J. Nesbitt<sup>b)</sup>

*JILA, University of Colorado and National Institute of Standards and Technology,  
and Department of Chemistry and Biochemistry, University of Colorado, Boulder, Colorado 80309-0440*

(Received 15 December 1998; accepted 2 February 1999)

Vibrationally mediated photodissociation dynamics of water on the first excited electronic state surface ( $\tilde{A}$ ) has been studied with slit jet-cooled H<sub>2</sub>O prepared in the complete polyad of  $\nu_{\text{OH}}=3$  overtone stretch levels ( $|03^+\rangle$ ,  $|12^+\rangle$ ,  $|12^-\rangle$ , and  $|03^-\rangle$ ). (Notationally,  $|n_1 n_2^\pm\rangle$  refers to symmetric/antisymmetric combinations of local mode OH stretch excitation, roughly corresponding to  $n_1$  and  $n_2$  quanta in the spectator and photolyzed OH bond, respectively.) At 248 nm photolysis wavelength the Condon point for bond cleavage occurs in the classically forbidden region, primarily sampling highly asymmetric H+OH *exit valley* geometries of the potential energy surface. Rotational, vibrational, spin orbit, and lambda doublet distributions resulting from this “far off resonance” photodissociation process are probed via laser induced fluorescence, exploiting the high efficiency laser excitation and light collection properties of the slit jet expansion geometry. Only vibrationally unexcited OH products are observed for both  $|12^\pm\rangle$  and  $|03^\pm\rangle$  initial excitation of H<sub>2</sub>O, despite different levels of vibration in the spectator OH bond. This is in contrast with “near-resonance” vibrationally mediated photolysis studies by Crim and co-workers in the  $|04^-\rangle$  and  $|13^-\rangle$  manifold, but entirely consistent with theoretical predictions from a simple two-dimensional quantum model. Photolysis out of the rotational *ground* H<sub>2</sub>O state (i.e.,  $J_{K_a K_c}=0_{00}$ ) yields OH product state distributions that demonstrate remarkable *insensitivity* to the initial choice of H<sub>2</sub>O vibrational stretch state, in good agreement with rotational Franck–Condon models. However, this simple trend is not followed uniformly for rotationally *excited* H<sub>2</sub>O precursors, which indicates that these Franck–Condon models are insufficient and suggests that exit channel interactions do play a significant role in photodissociation dynamics of H<sub>2</sub>O at the fully state-to-state level. © 1999 American Institute of Physics. [S0021-9606(99)00517-6]

## I. INTRODUCTION

As one of the simplest paradigms of chemical bond breaking, the dynamics of photodissociation has long been an important focus of chemical physics research, both from experimental and theoretical points of view.<sup>1–12</sup> The photodissociation of H<sub>2</sub>O in its first absorption band, a classic yet tractable triatomic system, has received particularly extensive attention over the past decade.<sup>1–12</sup> Stimulated in large measure by close interaction between theory and experiment, H<sub>2</sub>O has effectively become the benchmark system for direct unimolecular dissociation on a single repulsive electronic potential energy surface (PES). As one example of astrophysical significance, H<sub>2</sub>O photolysis has been speculated to be responsible for generating  $\Lambda$ -doublet population inversions evident in interstellar OH maser emission phenomena.<sup>3,4</sup> Of special importance in promoting strong interaction between theory and experiment has been the development of multiple resonance methods<sup>3,5–12</sup> to control the initial photolysis state of H<sub>2</sub>O. Specifically, these methods permit investigation of

H–OH bond breaking dynamics from fully labeled quantum states and the subsequent evolution of excess energy into translational, rotational, vibrational, and electronic degrees of freedom of the H and OH products.

In the pioneering vibrationally mediated photolysis experiments of Andresen and co-workers and Crim and co-workers, a single quantum state of H<sub>2</sub>O is selected by near infrared (IR) or visible overtone excitation prior to ultraviolet (UV) dissociation and the distribution of final quantum states is probed via laser induced fluorescence (LIF) on the OH product.<sup>3,9–12</sup> Experimental access to such levels of state-to-state detail is greatly facilitated in H<sub>2</sub>O for several reasons. First of all, the large energy spacing in the OH stretch manifold in water ( $\Delta\nu\approx 3700\text{ cm}^{-1}$ ) permits isolated quantum states of H<sub>2</sub>O at chemically significant energies to be accessed via low overtone vibrational pumping. In conjunction with a 248 nm UV photolysis wavelength, this permits rigorously background free cleavage of the H–OH bond from a specific rovibrational state. Second, the first excited electronic state of H<sub>2</sub>O is purely repulsive, therefore excitation results in rapid dissociation into photoproducts formed exclusively in the lowest electronic states, i.e., H(<sup>1</sup>S) and OH(<sup>2</sup>Π).<sup>4,13</sup> Third, outside of fine structure interactions, there are no curve crossings with this lowest surface to form

<sup>a)</sup>Present address: National Institute for Standards and Technology Gaithersburg, MD 20899.

<sup>b)</sup>Staff member, Quantum Physics Division, National Institute of Standards and Technology; electronic mail: djn@jila.colorado.edu

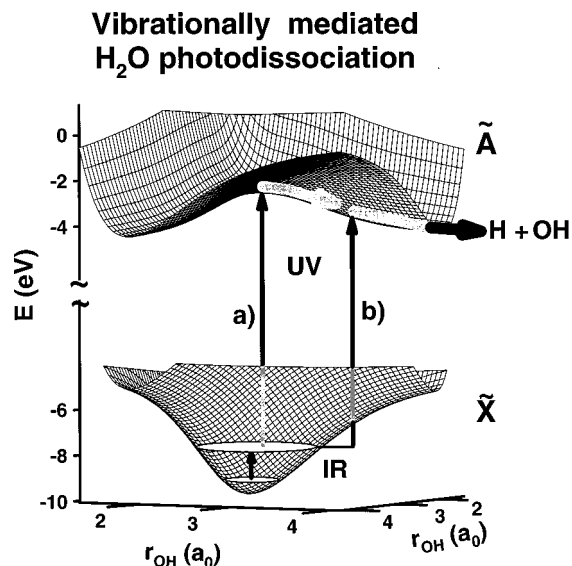


FIG. 1. Pictorial representation of vibrationally mediated photodissociation of  $\text{H}_2\text{O}$ . The photodissociation event is initiated by UV laser excitation from a specific laser selected overtone level of ground electronic state  $\tilde{X}$  and the repulsive excited electronic state  $\tilde{A}$ . The energy of the photolysis photon determines the regions of the  $\tilde{A}$  PES sampled in the photodissociation process. At higher photon energies (a), regions near the saddle point are energetically accessed, while at lower photon energies (b), only potential surface regions far out in the exit channel are sampled significantly.

higher electronic states such as  $\text{OH}(^2\Sigma)$  manifold, making complications due to nonadiabatic processes unlikely. Finally, the nascent distributions of vibrational, rotational, spin orbit, and lambda doublet states of OH can be detected with high experimental sensitivity via LIF.<sup>14,15</sup>

From a theoretical perspective, the electronic structure of  $\text{H}_2\text{O}$  is accessible to high level *ab initio* calculations and thus a reliable PES for the repulsive electronic state is available.<sup>16</sup> At the same time, dynamics capabilities have progressed to a point where fully rigorous quantum dynamics of triatomic photodissociation phenomena can now be calculated. Indeed, quantum time independent<sup>17–19</sup> and wave-packet propagation calculations<sup>20–22</sup> have been successfully performed on  $\text{H}_2\text{O}$  photolysis with few or no dynamical approximations. This special combination of capabilities makes possible unprecedentedly refined investigations of the triatomic photodissociation event, providing explicit theoretical predictions for experimental observables such as photolysis cross sections or product state distributions.

The vibrationally mediated photodissociation process is schematically illustrated in Fig. 1. An IR photon excites a specific rovibrational state on the ground electronic PES, followed by selective UV excitation to the excited electronic state and prompt dissociation to products. As is especially important in the present studies, the choice of IR and UV photon energies qualitatively controls the regions of the  $\tilde{A}$  PES sampled in the photodissociation process. For example, ‘‘on-resonance’’ excitation [marked (a) in Fig. 1] reflects a situation where the photons provide enough energy to reach the saddle point region, whereas for ‘‘far off resonance’’ excitation at longer wavelengths [marked (b) in Fig. 1], the initial  $\text{H}_2\text{O}$  wave function is localized to the lower energy

exit channel portion of the  $\tilde{A}$  PES. Alternatively stated, Fig. 1(a) illustrates excitation in the Franck–Condon region, predominantly sampling the classically *allowed* portion of the vibrational wave function, while Fig. 1(b) illustrates non-Franck–Condon excitation where the classically *forbidden* wings of the vibrational wave function are primarily responsible for the absorption event.

Inspection of the  $\tilde{A}$  state PES reveals several features that are unique to the  $\text{H}_2\text{O}$  system and simplify the dissociation dynamics considerably. First of all, as the dissociating O–H bond length increases, both the equilibrium bond distance and the diatomic force constant of the spectator OH change only slightly. Consequently, to a first approximation, the photodissociation process is anticipated to be vibrationally adiabatic, i.e., conserving the number of quanta of initial  $\text{H}_2\text{O}$  vibrational excitation in the spectator OH bond. Indeed, this is the major reason why  $\text{H}_2\text{O}$  has proven to be such an excellent system for mode selective photochemistry, i.e., controlled UV cleavage of a specific molecular bond by vibrational excitation. Classic studies by Crim and co-workers,<sup>12</sup> for example, have demonstrated that photolysis of the  $|04^- \rangle$  state of  $\text{H}_2\text{O}$  (i.e., the antisymmetric combination of local mode states with zero and four quanta of OH stretching excitation, respectively) yields OH fragments predominantly in the  $v_{\text{OH}}=0$  vibrational state, whereas mostly  $v_{\text{OH}}=1$  is produced from photolysis of the  $|13^- \rangle$  state. These experiments indicate that the vibrationally tagged OH bond with higher local mode vibrational excitation dissociates preferentially, while vibrational excitation in the remaining OH bond is adiabatically conserved during the dissociation.

The partial cross sections for different OH vibrational states have been calculated for several initial vibrational states of  $\text{H}_2\text{O}$  including  $|04^- \rangle$  and  $|13^- \rangle$  using both time independent<sup>19</sup> and time dependent wave-packet propagation methods,<sup>21,22</sup> with results in nearly quantitative agreement with experimental data. However, these calculations also indicate that the simple physical picture described above for preferential bond cleavage and vibrational adiabaticity is valid only for a range of photolysis energies near the saddle point between the two H–OH and HO–H channels on the  $\tilde{A}$  state PES. Thus, at low photolysis energies it has been suggested<sup>21</sup> that production of the ground vibrational states of the OH should become the dominant channel regardless of initial  $\text{H}_2\text{O}$  vibrational state, even though higher vibrational states of OH may still be energetically accessible. This can be directly tested by vibrationally mediated photolysis of  $\text{H}_2\text{O}$  at lower overtone levels and longer photolysis wavelengths, which forms one focus of the present studies.

The rotational distributions of the OH fragment also provide detailed information on the photodissociation process and opportunities for comparison between experiment and theoretical predictions. From *ab initio* calculations, the equilibrium H–O–H bond angle for the  $\tilde{A}$  state is similar to the  $\tilde{X}$  state and does not change considerably as the dissociating OH bond is stretched.<sup>16</sup> As a result, the OH fragment is expected to experience only minor torques while rolling out

the exit channel, i.e., qualitatively consistent with the relatively cold distribution of rotational states experimentally observed. It is worth noting that this is not simply due to energetics; the rotational states populated reflect only  $\approx 1\%$ – $2\%$  of the total excess energy available from photolysis. More quantitatively, detailed theoretical studies of rotational distributions have been carried out by Schinke, Engel, and Staemmler,<sup>18</sup> based on the rotational Franck–Condon model originally developed by Balint-Kurti.<sup>23</sup> In this model, all such “exit channel interactions” are explicitly neglected, for example, those arising from differences in ground and electronically excited state bending potentials, bend–stretch or rotation–vibration coupling, as well as recoil torques between the receding H and OH fragments. In this Franck–Condon approximation, the rotational distributions are predicted simply by expanding the initial rovibrational bending wave function of H<sub>2</sub>O in a complete set of free rotational states of the OH fragment. Despite the simplicity of these assumptions, this model has yielded surprisingly reasonable agreement with experiment in many previous studies.<sup>3,10,12</sup> However, recent vibrationally mediated photodissociation work of Brouard and Langford for both H<sub>2</sub>O and HOD has begun to reveal significant discrepancies from these rotational Franck–Condon predictions, which have therefore been modified to incorporate exit channel interactions such as dynamical torques on the OH fragment during the dissociation event.<sup>6,7</sup>

In this work we investigate the vibrationally mediated photodissociation dynamics of  $\nu_{\text{OH}}=3$  excited H<sub>2</sub>O at 248 nm. The combination of second overtone vibrational excitation in water combined with a 248 nm photodissociation wavelength yields a total photolysis energy that is  $4500\text{ cm}^{-1}$  below the saddle point on the  $\tilde{A}$  PES, i.e., sampling the far off resonance regime. From a semiclassical Condon point perspective, this corresponds to photolysis from a highly asymmetrical H<sub>2</sub>O molecule, with one bond differentially elongated by  $0.4\text{ \AA}$  and consequently strongly skewed toward the exit channel region of the upper surface. One focus of this work is to determine the OH product vibrational distributions as a function of the initial vibrational state of H<sub>2</sub>O ( $|03^+\rangle, |03^-\rangle, |12^+\rangle, |12^-\rangle$ ) as well as relative photolysis cross sections out of these vibrationally mediated target states. A secondary focus is to provide OH rotational, spin orbit, and lambda doublet distributions for 248 nm photolysis from selected H<sub>2</sub>O intermediate rotational ( $J_{K_a K_c}=0_{00}, 1_{01}, 1_{10}, 1_{11}, 2_{02}, 2_{12}, 2_{20}$ ) and vibrational ( $|03^+\rangle, |03^-\rangle, |12^+\rangle, |12^-\rangle$ ) states accessible via excitation out of  $0_{00}$  (para) and  $1_{01}$  (ortho) lower state levels populated under jet cooled conditions. This represents a study of vibrationally mediated photolysis of H<sub>2</sub>O out of the  $\nu_{\text{OH}}=3$  stretch manifold, which therefore nicely complements previous experiments obtained for  $\nu_{\text{OH}}=1, 4,$  and  $5$  vibrational excitation, both at total photolysis energies comparable to our experiment<sup>6,7</sup> and at higher photolysis energies.<sup>3,8,10,12</sup>

The rest of the article is organized as follows. Section II provides the experimental details relevant to the present work. The results of OH product vibrational distributions and relative photolysis cross sections for the overtone manifold of  $\nu_{\text{OH}}=3$  initial H<sub>2</sub>O states are summarized in Sec. III and

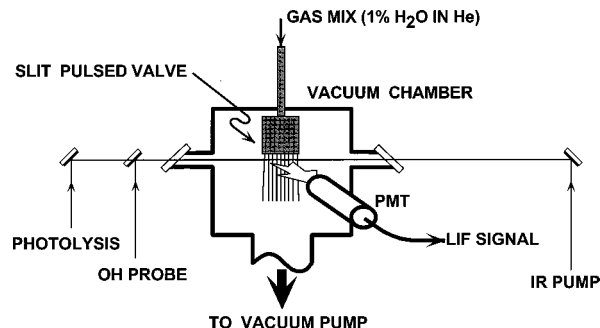


FIG. 2. Schematic of the experimental apparatus. Jet-cooled H<sub>2</sub>O molecules are introduced to the photolysis and probe region via slit supersonic expansion. The molecular beam is intersected along the slit axis by a series of three laser pulses. (1) A single rovibrational state is selected with a single model OPO operating in the  $\nu_{\text{OH}}=3\leftarrow 0$  overtone region. (2) The selected state is photolyzed by an UV pulse at 248 nm wavelength temporally coincident with the IR pulse. (3) The OH products are probed via LIF at 308 nm after a 200 ns time delay, with the LIF signal detected by a PMT normal to the slit expansion plane.

interpreted by comparison with results from a simple two-dimensional (2D) Franck–Condon analysis. In Sec. IV, we present OH rotational, spin orbit and lambda doublet distributions for photolysis at 248 nm and make comparisons with the results of previous initial rotational quantum state resolved photolysis studies in the  $\nu_{\text{OH}}=1, 4,$  and  $5$  manifolds. For the rotationless ( $0_{00}$ ) state, these comparisons underscore the remarkable *insensitivity* of OH rotational state distributions to initial H<sub>2</sub>O vibrational state. For higher initial rotational states, however, these results reveal a more dramatic and selective dependence on the H<sub>2</sub>O vibrational state, which suggest a more complicated role of exit channel interactions in the photolysis event. The conclusions of the article are summarized in Sec. V.

## II. EXPERIMENT

The experimental techniques used in the present study for photolysis of  $\nu_{\text{OH}}=3$  excited H<sub>2</sub>O are based on the vibrationally mediated photodissociation methods of Hausler, Andresen, and Schinke<sup>3</sup> and Crim and co-workers,<sup>10,12</sup> modified for enhanced sensitivity in a low density supersonic jet environment. The key components of the experimental apparatus are summarized in Fig. 2. A slit supersonic expansion is used to cool H<sub>2</sub>O molecules into the lowest rotational levels allowed by nuclear spin statistics, i.e.,  $J_{K_a K_c}=0_{00}$  (para) and  $1_{01}$  (ortho). The jet cooled H<sub>2</sub>O molecules are then pumped into specific rovibrational states in the  $\nu_{\text{OH}}=3$  OH stretch overtone manifold by IR pump pulses from a single mode, tunable optical parametric oscillator (OPO), which in turn are selectively photodissociated by a KrF excimer laser pulse at 248 nm. Finally, the nascent OH product distributions resulting from the state-selected photolysis events are probed under collision free conditions by LIF methods optimized for the slit jet configuration. Some relevant experimental details are provided below.

The H<sub>2</sub>O supersonic expansion sample is introduced into the vacuum chamber through a pulsed slit nozzle ( $4\text{ cm}\times 50\text{ }\mu\text{m}$ ,  $500\text{ }\mu\text{s}$  pulse duration), with typically  $0.5\%$ – $1\%$  of H<sub>2</sub>O seeded in a carrier gas (He, Ne, or Ar) at

a total stagnation pressure of 200–600 Torr. Due to rotational cooling in the supersonic expansion, the H<sub>2</sub>O populations are concentrated into the lowest ortho ( $1_{01}$ ) and para ( $0_{00}$ ) rotational states in the 3:1 ratio dictated by the nuclear spin statistics. As a result of the slower ( $1/r$ ) drop off in gas density, the slit expansion provides high concentrations of H<sub>2</sub>O per quantum state in the interaction region and also provides a long absorption path for enhancing weak overtone transition probabilities. Furthermore, the slit geometry results in efficient collimation of velocities along the slit axis, which leads to an order of magnitude narrowing of overtone Doppler widths and thus a corresponding enhancement of vibrationally mediated photodissociation signals for a sub-Doppler pump laser. The LIF detection volume (1 mm  $\times$  1 mm  $\times$  4 cm) is spatially filtered and imaged onto the photomultiplier tube (PMT), using light collection assembly optics described elsewhere for high scattered light rejection ( $1:10^9$ ) and high efficiency ( $\approx 10\%$ ) collection along the slit dimension.<sup>24</sup>

A single mode injection seeded OPO of our own design<sup>25</sup> serves to select single rovibrational states in the  $\nu_{\text{OH}}=3$  stretching manifold. The OPO is based on a four mirror ring cavity resonator, with a matched pair of beta barium borate (BBO) crystals pumped at 355 nm from a frequency tripled, single-mode, injection seeded neodymium:yttrium–aluminum–garnet (Nd:YAG) laser to produce high spectral brightness (5–10 mJ) signal and idler pulses in the visible (570–650 nm) and near-IR (790–950 nm) spectral region, respectively. By injection seeding the BBO resonator with a single-mode continuous wave dye laser, a Fourier-transform limited output of the ring OPO is achieved with a spectral width of 160 MHz ( $\approx 0.005 \text{ cm}^{-1}$ ), averaged over multiple pulses. With output pulse energies of  $\geq 5$  mJ/pulse, this OPO light source provides sufficient spectral brightness to partially saturate up to  $\Delta\nu = 3$  OH stretch overtone rovibrational transitions. With efficient jet cooling into the lowest two rotational levels, this permits significant optical pumping (10%–20%) of the total H<sub>2</sub>O molecules in the probe volume into a given rovibrational quantum state. For typical stagnation pressures and distances downstream from the slit nozzle, this translates into excited state H<sub>2</sub>O densities in excess of  $10^{13}$  molecules/cm<sup>3</sup> and  $4 \times 10^{11}$  total molecules in the detection volume, respectively.

Due to high spectral resolution of the OPO pump source and sub-Doppler linewidths in the slit expansion geometry, the long term frequency stability of the OPO output is critical. Specifically, even a relatively small frequency drift ( $\approx 100$  MHz) during the course of an experiment would tune the laser off the molecular transition and consequently lead to loss of multiple-resonance signals. Active servo-loop methods for OPO frequency stabilization are based on locking the stabilized optical transfer cavity onto the output of a polarization stabilized He–Ne laser followed by locking both (i) the injection seed dye laser for the OPO and (ii) injection seed diode laser for the Nd:YAG onto the same stabilized transfer cavity. With this procedure, one can achieve frequency drifts in the OPO output of less than  $\pm 20$  MHz over a period of several hours,<sup>26</sup> which proves entirely adequate for present purposes.

TABLE I. Experimentally observed  $\nu_{\text{OH}}=1/\nu_{\text{OH}}=0$  branching ratios obtained via vibrationally mediated photolysis of H<sub>2</sub>O pre-excited into  $\nu_{\text{OH}}=3$  (this work) and  $\nu_{\text{OH}}=4$  [Crim and co-workers (Ref. 10)] overtone manifolds. Note the strong decrease in  $\nu_{\text{OH}}=1$  vs  $\nu_{\text{OH}}=0$  populations with decreasing photolysis excess energy, i.e., exciting further out in the exit channel of the potential energy surface.

H <sub>2</sub> O state	Photolysis wavelength (nm)	Excess energy (cm <sup>-1</sup> )	$\nu_{\text{OH}}=1/\nu_{\text{OH}}=0$
$ 03^- \rangle$	248	9000	<1:200
$ 04^- \rangle$	239.5	13 600	1:100
$ 04^- \rangle$	218.5	17 600	1:10
$ 12^- \rangle$	248	9400	<1:50
$ 13^- \rangle$	239.5	14 100	5.2:1
$ 13^- \rangle$	218.5	18 100	6:1

An excimer laser operating on KrF mix at 248 nm is used as the photolysis source, typically scaled down to 20 mJ/pulse in the jet region. The measured UV photolysis power dependence of the vibrationally mediated signals is linear and indicates no signs of optical saturation. This is consistent with the far off resonance nature of the vibrationally mediated photolysis process, which in more favorable cases yields UV cross sections more than two orders of magnitude smaller than peak values ( $\sigma \approx 10^{-18} \text{ cm}^2$ ) predicted in the Franck–Condon region. For typical UV pulse energies (20 mJ/pulse) and beam areas (1 mm<sup>2</sup>), this translates into  $\approx 4 \times 10^9$  photolyzed H<sub>2</sub>O molecules in the detection volume.

A conventional frequency doubled pulsed dye laser source provides tunable radiation near 308 nm to probe the  $\nu_{\text{OH}}=0 \leftarrow 0$  and  $1 \leftarrow 1$  sub-bands of the  $2^2\Sigma \leftarrow 2^2\Pi$  electronic transition in the OH product. To obtain reliable product state distributions from the obtained LIF spectra, one must compensate for LIF signal saturation effects. Specifically, at these OH photofragment densities in the jet expansion environment, it is difficult to obtain adequate signal-to-noise (S/N) for all OH transitions with sufficiently low probe powers to be rigorously in the linear regime. Thus, the UV probe laser is operated at typical energies of 2–20  $\mu\text{J}$ /pulse, a range over which the LIF signals begin to show slight curvature with increasing power due to partial saturation. This partial saturation behavior is corrected by calibrating the OH signals as a function of pulse energy against thermally equilibrated 300 K OH distributions, which are readily obtained in the same detection geometry by 193 nm photolysis of static H<sub>2</sub>O inert gas mixtures. As described elsewhere in detail, this procedure permits a quantitative mapping between observed signal strengths and OH population in given state, and allows one to obtain product state distributions<sup>24</sup> in a partially saturated regime.

### III. RESULTS AND ANALYSIS

As summarized in Table I, single-mode near-IR OPO excitation of a jet-cooled H<sub>2</sub>O sample is exploited to select a series of intermediate rotational states ( $J_{K_a K_c} = 0_{00}, 1_{01}, 1_{11}, 1_{10}, 2_{02}, 2_{12},$  and  $2_{20}$ ) in all four vibrational levels of the  $\nu_{\text{OH}}=3$ , OH stretch overtone manifold. Subsequent photolysis at 248 nm leads to H+OH products, preferentially

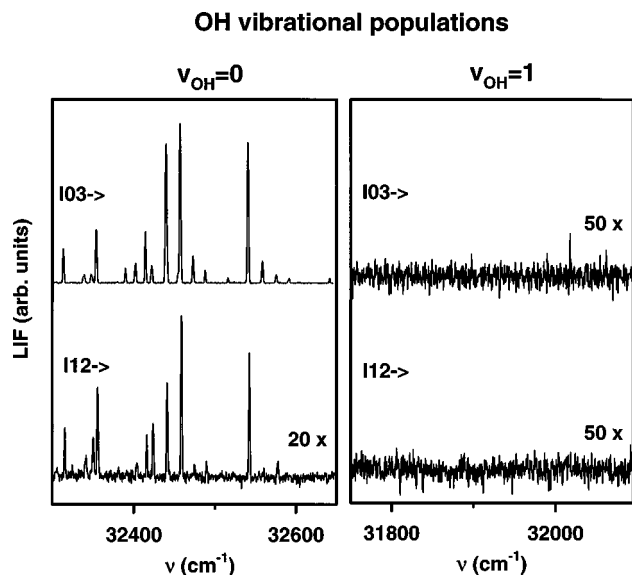


FIG. 3. Sample LIF spectra of OH products produced via vibrationally mediated photodissociation of  $\text{H}_2\text{O}$ . The OH products from  $|03^- \rangle$  and  $|12^- \rangle$  initial vibrational states of  $\text{H}_2\text{O}$  are reflected in the top and bottom panels, respectively. OH in its ground ( $v_{\text{OH}}=0$ ) and first excited ( $v_{\text{OH}}=1$ ) vibrational states are probed in the left hand and right hand panels, respectively. Note the lack of any OH ( $v=1$ ) nascent state population from photolysis of either  $|03^- \rangle$  or  $|12^- \rangle$ , despite the 50-fold increase in scale sensitivity.

sampling photofragmentation dynamics in the exit valley versus the inner Franck–Condon region (see Fig. 1). This combination of IR+UV photolysis wavelengths yields excess energies in the  $\text{H}+\text{OH}$  product on the order of  $\approx 9400 \text{ cm}^{-1}$ ; this is appreciably smaller than sampled in the previous vibrationally mediated photolysis studies of Crim and co-workers for  $v_{\text{OH}}=4$  (between  $14\,100$  and  $18\,100 \text{ cm}^{-1}$  for  $220\text{--}240 \text{ nm}$ )<sup>10,12</sup> and of Hausler, Andresen, and Schinke for  $v_{\text{OH}}=1$  ( $\approx 13\,900 \text{ cm}^{-1}$  for  $193 \text{ nm}$ ).<sup>3</sup> However, these excess product state energies are more comparable to those investigated by Brouard and co-workers,<sup>6,7</sup> who used  $282 \text{ nm}$  light as both the UV photolysis and OH probe laser to study vibrationally mediated photofragmentation dynamics of  $\text{H}_2\text{O}$   $v_{\text{OH}}=4$  and  $v_{\text{OH}}=5$  overtones, yielding excess energies of  $7700$  and  $10\,700 \text{ cm}^{-1}$ , respectively.

### A. OH vibrational distributions

The four panels in Fig. 3 represent LIF spectra probing the OH product state distributions from vibrationally mediated photodissociation of  $\text{H}_2\text{O}$ . In the left hand set of panels, the OH ground vibrational state population ( $v_{\text{OH}}=0$ ) is sampled via excitation on the  $v_{\text{OH}}=0 \leftarrow 0$  sub-band of the  ${}^2\Sigma \leftarrow {}^2\Pi$  electronic transition. In the right hand set of panels, the corresponding  $v_{\text{OH}}=1 \leftarrow 1$  sub-band region of the same electronic transition is presented, thus revealing the absence of any nascent population in the  $v_{\text{OH}}=1$  state. For the top two panels, the OPO IR excitation laser is tuned to the  $0_{00} \leftarrow 1_{01}$  rotational transition in the  $|03^- \rangle$  vibrational manifold of  $\text{H}_2\text{O}$ , i.e., an antisymmetric state with nominally three and zero quanta of local mode stretching vibration, respectively, localized in one of the two equivalent OH bonds. Conversely, for the lower two panels, the intermediate vibra-

tional state is  $|12^- \rangle$ , i.e., the antisymmetric combination of two and one quanta of local mode stretching excitation localized in the two OH bonds, respectively.

The data reveal several interesting results. First, only the  $v_{\text{OH}}=0$  ground vibrational state is observed at  $248 \text{ nm}$  photolysis wavelength, with an upper limit of  $<0.05\%$   $v_{\text{OH}}=1$  product within the S/N (note the 50-fold increase in scale sensitivity). Second and more importantly, this vanishingly small  $v_{\text{OH}}=0/v_{\text{OH}}=1$  ratio is observed for both  $|03^- \rangle$  and  $|12^- \rangle$  excitation, i.e., independent of the intermediate vibrational state of  $\text{H}_2\text{O}$ . It is important to note that this is not simply due to energetics, which would make vibrational states up to OH ( $v=3$ ) accessible. This is in contrast with previous observations at higher total photolysis energies,<sup>10</sup> which clearly demonstrate that vibrational excitation in the nondissociating “spectator” OH bond tends to be adiabatically conserved in the dissociation event. Specifically, a five-fold excess of *excited state*  $v_{\text{OH}}=1$  products were observed when the  $|13^- \rangle$  state was dissociated, while dissociation from the  $|04^- \rangle$  state led to predominantly *ground state*  $v_{\text{OH}}=0$  products. By way of comparison, Table I compares the present  $v_{\text{OH}}=0/v_{\text{OH}}=1$  branching ratios with those previously reported. The final feature worth noting is the order of magnitude *increase* in LIF signal intensity for  $|03^- \rangle$  versus  $|12^- \rangle$  vibrational excitation. Since the known overtone IR absorption cross sections are comparable for exciting these two states, this reflects significantly different photolysis cross sections for UV photodissociation out of these two vibrational levels.

More quantitatively, we obtain the relative photodissociation cross sections for each of the four intermediate rovibrational states of  $\text{H}_2\text{O}$  from the experimental data and compare it with predictions of a 2D quantum model discussed in Sec. III B. For extracting relative cross sections from the measured OH populations, one must take into account (i) the overtone transition probability to the intermediate state and (ii) the  $\text{H}_2\text{O}$  concentration in the initial quantum state. As discussed above, only the two lowest rotational states of  $\text{H}_2\text{O}$ ,  $0_{00}$ , and  $1_{01}$ , are populated in the free jet expansion, with a 1:3 population ratio dictated by nuclear spin statistics. In the unsaturated limit, the optical transition probability is proportional to the transition line strength, which is experimentally known from the HITRAN database.<sup>27</sup> Since the full spectral brightness of the infrared OPO is capable of partially saturating the second overtone vibrational transitions. The pulse energies are attenuated until  $\text{H}_2\text{O}$  photoacoustic signals scale linearly with power and transition line strength, i.e., verifying that saturation effects are negligible. The  $248 \text{ nm}$  photodissociation cross sections for photodissociation from  $|03^- \rangle$ ,  $|03^+ \rangle$ ,  $|12^- \rangle$ , and  $|12^+ \rangle$  states are found to be 1:3.0(15):0.08(3):0.17(5), respectively, with no dependence on intermediate rotational state within experimental uncertainty.

### B. 2D quantum theoretical model

To interpret these results, we have carried out simplified time independent quantum calculations of the final state resolved photodissociation cross sections. The model follows

the time independent approach by Engel, Schinke, and Staemmler,<sup>19</sup> which in turn is based on the Fermi golden rule

$$\sigma(\nu) = \frac{4\pi^2\nu g(\nu)}{3\hbar c} |\langle \Psi' | \mu | \Psi'' \rangle|^2. \quad (1)$$

In Eq. (1),  $\sigma(\nu)$  is the UV absorption cross section,  $\Psi''$  and  $\Psi'$  are the ground and excited wave functions, respectively,  $\nu$  is the frequency of the excitation photon,  $g(\nu)$  is the density of states, and  $\mu$  is the dipole moment operator. In the context of the Born–Oppenheimer approximation,  $\Psi''$  and  $\Psi'$  represent bound and continuum wave functions for the nuclear motion on the ground and excited PESs. Similarly,  $\mu$  is the electronic transition dipole moment vector as a function of intramolecular coordinates, as taken from the work of Staemmler and Palma.<sup>16</sup> Throughout this analysis, the upper state potential surface is also taken from the full three-dimensional (3D) *ab initio* PES by Staemmler and Palma,<sup>16</sup> while the potential surface of Sorbie and Murrell<sup>28</sup> is used for the ground state.

The following additional assumptions are implemented to simplify the analysis. First, the bending and stretching coordinates in H<sub>2</sub>O are assumed to be decoupled from each other, with the bend angle fixed at 104° for both ground and first excited electronic states. This approximation has been commonly invoked in previous theoretical treatments, based on small changes in the bending potentials between ground and excited electronic states. The ground state wave functions are then expanded in a direct product basis set of the two OH stretching coordinates and solved numerically via matrix diagonalization. Second, coupling between the two OH stretch degrees of freedom in the exit channel is neglected, i.e., the excited state potential surface is approximated by

$$V(R, r) = V_{\text{repulsive}}(R) + V_{\text{OH}}(r), \quad (2)$$

where  $r$  and  $R$  are Jacobi coordinates representing (i) the nondissociating OH bond length, and (ii) the distance between the OH center of mass and departing H atom, respectively. This assumption should be reasonably accurate for photolysis far into the exit channel, where the coupling between OH vibration and H–OH translation is weak. Consistent with this approximation,  $V_{\text{repulsive}}(R)$  is determined from the minimum energy of  $V(R, r)$  with respect to  $r$ , obtained parametrically as a function of  $R$ , while  $V_{\text{OH}}(r)$  is simply taken to be  $V(R, r)$  at asymptotically large values of  $R$ .

Within the context of these two assumptions, the total excited state wave function can be expressed as

$$\Psi'(R, r) \approx \psi_\epsilon(R) \phi_\nu(r), \quad (3)$$

where  $\phi_\nu(r)$  is the  $\nu$ th vibrational wave function of free OH and  $\psi_\epsilon(R)$  is the one-dimensional (1D) scattering wave function satisfying the following Schrödinger equation:

$$\left( \frac{-\hbar^2}{2\mu} \frac{\partial^2}{\partial R^2} + V_{\text{repulsive}}(R) \right) \psi_\epsilon = \epsilon \psi_\epsilon. \quad (4)$$

In Eqs. (3) and (4),  $\epsilon$  is the asymptotic center of mass translational energy for a given scattering wave function, which in conjunction with the internal vibrational energy of departing OH product requires a total energy of  $E_{\text{tot}} = \epsilon + E_{\text{OH}}$ . For

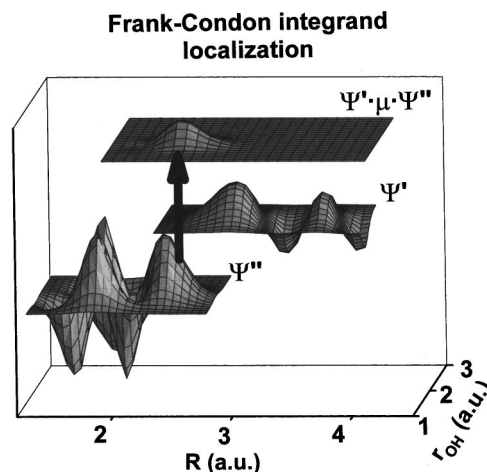


FIG. 4. Sample matrix element overlap between the ground state vibrational wave function  $\Psi''$   $|03^- \rangle$  and the scattering wave function  $\Psi'$  [ $\text{OH}(\nu=0)$ ]. The resulting dipole moment integrand  $\Psi' \mu \Psi''$  is strongly localized in the optimal overlap region between those two wave functions, which for these excess energies leads to Franck–Condon factors sensitive to the outgoing  $\text{OH}(\nu)$  state.

a given lower state potential and intermediate rovibrational state, this value of  $E_{\text{tot}}$  is supplied by the UV photolysis energy, which uniquely determines  $\epsilon$  for each separate  $\text{OH}(\nu)$  vibrational channel.

In this model, both  $\phi_\nu(r)$  and  $\psi_\epsilon(R)$  are 1D wave functions that can be readily obtained by a number of numerical methods. For calculational simplicity, the wave functions are solved variationally in a basis set of harmonic oscillator eigenfunctions for the lower state and a grid of distributed Gaussians for the upper state followed by matrix diagonalization. To make the wave function normalization in Eq. (1) consistent between lower (bound) and upper (continuum) states, the continuum solutions for  $V_{\text{repulsive}}(R)$  are transformed to a discrete but energetically closely spaced set of bound-state solutions by adding a repulsive wall at large values of  $R=R_w$ . This procedure generates solutions only for discrete values of the excess energy  $\epsilon$ , but with a density of states  $g(\nu)$  that also depends on  $R_w$ . As a result, the transition dipole moment matrix element  $\langle \Psi' | \mu | \Psi'' \rangle$  decreases with increasing displacement of the outer wall, but is exactly compensated by a corresponding increase  $g(\nu)$  for sufficiently large  $R_w$ . The basis set is then successively increased in size until the calculated absorption cross sections defined by Eq. (1) are converged to at least three significant figures.

### C. Discussion

From Eq. (1), the predicted absorption cross sections are obtained from integration of  $\Psi' \mu \Psi''$  over all space; it is therefore instructive to observe the behavior of the dipole moment integrand itself. This is demonstrated in Fig. 4 for the  $|03^- \rangle$  ground vibrational wave function and the scattering wave function corresponding to 248 nm photodissociation and OH production in  $\nu_{\text{OH}}=0$ . As anticipated, the integrand is strongly localized in the exit channel region near the outer turning point of the ground state wave function  $\Psi''$ , i.e., with the nonspectator OH bond highly extended. If one

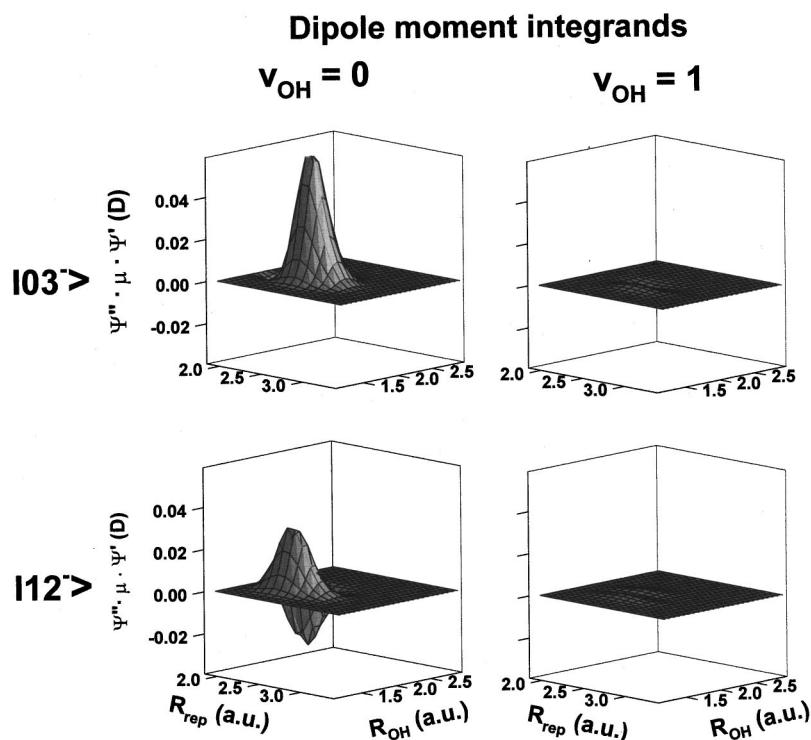


FIG. 5. Dipole moment integrand for initial H<sub>2</sub>O states  $|03^- \rangle$  and  $|12^- \rangle$  and final OH vibrational states  $v_{OH} = 0$  and  $v_{OH} = 1$ .

neglects any coordinate dependence of the dipole moment operator, this peaking of the dipole moment integrand occurs semiclassically at the Condon point, i.e., the stationary point for which the momentum of the particle is the same on both the ground and excited PES.<sup>29</sup> For higher photolysis energies (and thus higher values of  $E_{tot}$ ) the inner lobe of the scattering wave function shifts to progressively lower values of  $R$ , exponentially increasing overlap with the ground state wave function and therefore the amplitude of the dipole moment integrand.

This 2D quantum analysis provides a simple qualitative picture for the experimentally observed trends in  $v_{OH} = 0$  and  $v_{OH} = 1$  partial photodissociation cross sections. Figure 5 demonstrates this by plotting dipole moment integrands for 248 nm photolysis of the two H<sub>2</sub>O vibrational states  $|03^- \rangle$  and  $|12^- \rangle$ , projected onto the asymptotic H+OH continuum wave functions for  $v_{OH} = 0$  and 1. This combination is chosen explicitly for illustrative comparison with the experimental observations presented in Fig. 3. The integrated amplitudes are significantly lower for the  $v_{OH} = 1$  channels for both the  $|03^- \rangle$  and  $|12^- \rangle$  initial states, consistent with experimental observation that OH production in  $v_{OH} = 1$  is down from  $v_{OH} = 0$  by at least 50- to 100-fold. The reason for this is straightforward; for  $v_{OH} = 1$  the excess translational energy available to the fragments is reduced by an additional  $\approx 3700$  cm<sup>-1</sup>. Thus, the inner turning point of the scattering wave function is shifted to larger values of  $R$ , which exponentially diminishes Franck–Condon overlap with the ground state wave function and partial absorption cross section into  $v_{OH} = 1$ .

More subtly, these plots of dipole moment integrands also explain the strong decrease in total absorption cross section between the  $|03^\pm \rangle$  and  $|12^\pm \rangle$  states. Although the absolute values of the wave function amplitudes are comparable

for these two pairs of intermediate levels, the  $|12^\pm \rangle$  states exhibit a nodal plane in the  $r$  coordinate, which in a local mode picture corresponds to one quantum of vibrational excitation in the spectator OH bond. When integrated over the intermediate vibrational state wave function, this leads to significant cancellation in the Franck–Condon overlap and therefore predicts much lower UV photolysis cross sections for  $|12^\pm \rangle$  than  $|03^\pm \rangle$ .

A more quantitative comparison of calculated versus observed cross sections into  $v_{OH} = 0$  for all four initial vibrational states,  $|12^\pm \rangle$  and  $|03^\pm \rangle$  is summarized in Fig. 6. Considering the simplicity of the 2D model, the agreement is

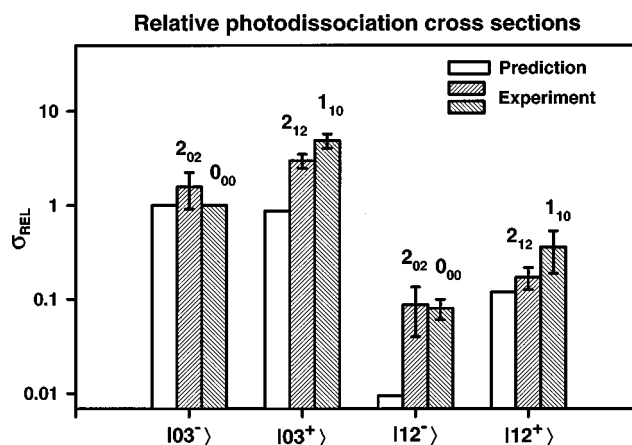


FIG. 6. Measured and calculated relative photodissociation cross sections at 248 nm, for each of the four initial H<sub>2</sub>O vibrational states probed in the experiment ( $|03^- \rangle$ ,  $|03^+ \rangle$ ,  $|12^- \rangle$ ,  $|12^+ \rangle$ ). Two different rotational states have been included for each vibrational state to demonstrate that photodissociation cross sections do not depend significantly on the initial rotational state, within experimental uncertainty.

reasonable and captures several of the experimental trends observed. Specifically, the 248 nm photolysis cross sections are predicted to be comparable for each of the  $|03^+\rangle$  and  $|03^-\rangle$  states, in good agreement with the 3.0(15) ratio observed experimentally. Furthermore, each of the  $|12^+\rangle$  and  $|12^-\rangle$  states are predicted to have 10- to 100-fold diminished UV absorption cross sections with respect to  $|03^+\rangle$  and  $|03^-\rangle$ , due to quantum interference in the dipole moment integrand, again in good qualitative agreement with experiment. In fact, the  $|12^-\rangle$  cross section is predicted to be almost an additional order of magnitude *lower* than observed experimentally. However, this is a result of quantum interference effects, which for near perfect cancellation in the dipole moment integral depend quite sensitively on both the model and details of the upper/lower potential surfaces. It would be of interest to calculate these relative absorption cross sections via a full 3D quantum model, and thereby permit a more rigorous test of the associated upper/lower potential surfaces. Finally, it is worth noting that at shorter wavelengths that access the Franck–Condon region directly, this 2D model also predicts photolysis trends analogous to those observed for the  $|13^-\rangle$  and  $|04^-\rangle$  initial states. Specifically, the  $v_{\text{OH}}=1$  channel becomes dominant for  $|12^-\rangle$  while for  $|03^-\rangle$ , production of  $v_{\text{OH}}=0$  remains the majority channel.

#### IV. OH PRODUCT STATE DISTRIBUTIONS

The presence of an unpaired electron in the  $^2\Pi$  state of OH leads to spin and orbital angular momentum contributions to the total angular momentum. The two spin-orbit states (labeled  $^2\Pi_{1/2}$  and  $^2\Pi_{3/2}$ ) are further split by coupling between electronic angular momentum and the end-over-end rotation into two  $\Lambda$ -doublet components, denoted by  $+/-$  superscripts according to the electronic wave function symmetry with respect to the OH end-over-end rotational plane. As a result of optical selection rules between the fine structure components, the rotational state populations in these four spin-orbit/ $\Lambda$ -doublet states can be extracted from  $Q$  and  $P/R$  branch analysis of the LIF spectrum of the OH photolysis product.<sup>15</sup> In practice, quantitative extraction of  $\Pi_{1/2}^-$  populations is not easily obtained due to overlapping  $Q$  branch lines at low  $N$ . However, all three other fine structure states ( $\Pi_{3/2}^+$ ,  $\Pi_{3/2}^-$ , and  $\Pi_{1/2}^+$ ) can be readily resolved and analyzed to yield relative populations of product OH.

The OH product state distributions have been determined for each rotational state accessible under jet cooled conditions for the four stretching vibrational states in the  $v_{\text{OH}}=3$  overtone manifold. As a result of the low slit jet temperatures and angular momentum considerations, the intermediate rotational states for vibrationally mediated photolysis are constrained to  $J \leq 2$  for single photon transitions. Furthermore, the  $+/-$  symmetry of  $\text{H}_2\text{O}$  overtone vibrational levels permits only  $A$ -type (i.e.,  $\Delta K_a = \text{even}$ ,  $\Delta K_c = \text{odd}$ ) and  $B$ -type (i.e.,  $\Delta K_a = \text{odd}$ ,  $\Delta K_c = \text{odd}$ ) transitions. Consequently, for the antisymmetric vibrational states ( $|03^-\rangle$  and  $|12^-\rangle$ ), vibrationally mediated photolysis out of  $0_{00}$ ,  $1_{01}$ ,  $2_{02}$ , and  $2_{20}$  rotational levels can be investigated, whereas for the symmetric vibrational states ( $|03^+\rangle$  and

$|12^+\rangle$ ), one can monitor the complementary  $1_{10}$ ,  $1_{11}$ , and  $2_{12}$  rotational levels. Experimental data have been obtained and analyzed on each of these intermediate states, the results of which are summarized in Table II and graphically presented in Figs. 7(a)–7(d).

The most dominant feature of the nascent OH rotational distributions is the large, nonmonotonic behavior in the populations. This effect is most clearly evident for low  $N$  quantum states, where the populations alternate with OH( $v, N$ ) rotational level and occur with opposite phase for the two  $\Lambda$ -doublet ( $^2\Pi_{3/2}^+$  and  $^2\Pi_{3/2}^-$ ) components. Such oscillations are due to quantum interference between the intermediate  $\text{H}_2\text{O}$  and final OH wave functions, where both nuclear and electronic degrees of freedom are included. Conversely, the qualitative trends observed for the two spin-orbit ( $^2\Pi_{3/2}^+$  and  $^2\Pi_{1/2}^+$ ) distributions are very similar; in fact, the two spin-orbit components at low  $N$  are often close to the 2:1 ratio predicted in the limit of a statistical dissociation. Both the strongly *nonstatistical* out of phase oscillations between  $\Lambda$ -doublet components and the nearly *statistical* ratios between spin-orbit manifolds have been observed in previous vibrationally mediated photolysis studies of the other overtone manifolds. Furthermore, there has been reasonable success at predicting many qualitative features of these highly structured distributions by Hausler, Andresen, and Schinke<sup>3</sup> based on rotational Franck–Condon models of Balint-Kurti.<sup>23</sup>

It has also been noted in previous studies of the  $v_{\text{OH}}=1, 4,$  and  $5$  vibrational manifolds that the OH rotational and fine structure distributions are insensitive to the nature of the intermediate vibrational state.<sup>3,10,12</sup> As rather dramatically shown in Fig. 8, the current study of the  $v_{\text{OH}}=3$  overtone manifold for  $|03^\pm\rangle$  and  $|12^\pm\rangle$  provides strong support of this trend for the rotationless ground state (though specific discrepancies in selected  $J>0$  levels will be mentioned later). Such behavior is of course consistent with the Franck–Condon model, in which the predicted OH rotational distributions solely reflect an expansion of the zero point bending wave function for  $\text{H}_2\text{O}$  in asymptotic free rotor OH states. Specifically, in the absence of such exit channel interactions as bend–stretch coupling, rotation–vibration mixing, recoil torques, and other dynamical effects that could be influenced by pre-excitation of the OH bond, the model predictions should be completely insensitive to the initial overtone vibrational state. However, this experimental trend has been argued by Brouard and co-workers<sup>6,7</sup> not to be due simply to a lack of such exit channel effects, but rather to a fortuitous balancing between (i) softening of the HOH bending potential and (ii) increase in the moment of inertia due to prestretching of the OH bond. If this is in fact the case, one might anticipate the insensitivity to overtone vibrational state for  $J_{K_a K_c}=0_{00}$  displayed in Fig. 8 to be less predictively reliable for rotationally excited  $\text{H}_2\text{O}$  levels.

Indeed, the OH product state behavior for  $v_{\text{OH}}=3$  photodissociation of  $\text{H}_2\text{O}$  molecules in  $J>0$  is more complicated. As demonstrated in Fig. 9 for  $J_{K_a K_c}=1_{10}$ , the initial vibration appears to play only a modest role in determining OH product state distributions, qualitatively similar to what is observed for the photolysis of the rotationless ground state

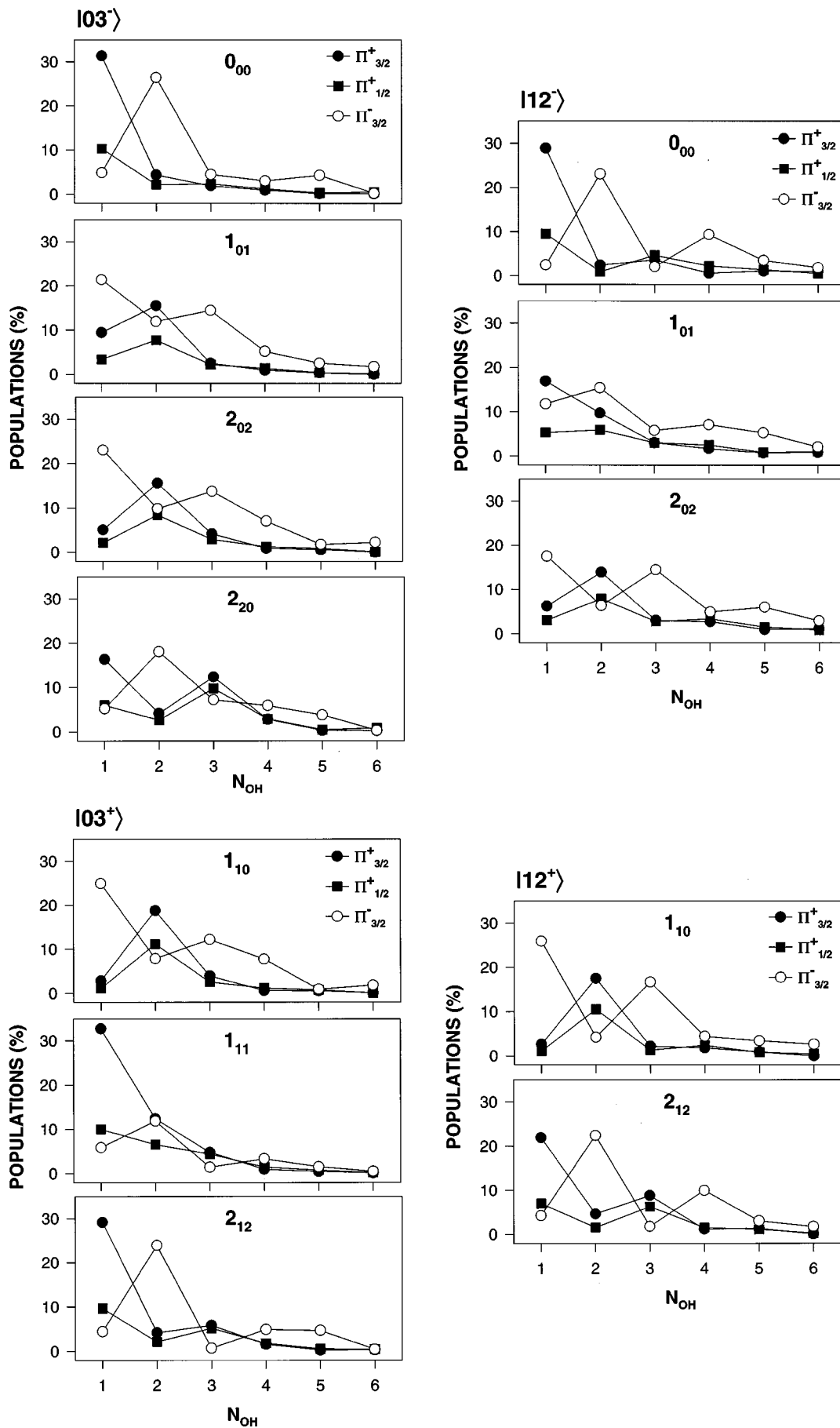


FIG. 7. Rotational, spin-orbit, and  $\Lambda$ -doublet distributions of the OH product for selected initial  $\text{H}_2\text{O}$  vibrational and rotational states: (a)  $|03^- \rangle$ , (b)  $|12^- \rangle$ , (c)  $|03^+ \rangle$ , and (d)  $|12^+ \rangle$ .

TABLE II. Fractional OH photofragment populations in rotational, spin-orbit, and lambda doublet states obtained from vibrationally mediated photolysis of all intermediate rovibrational states in the  $v_{\text{OH}}=3$  overtone manifold optically accessible from  $J_{K_a K_c}=0_{00}$  (para) and  $1_{01}$  (ortho)  $\text{H}_2\text{O}$  levels populated in the slit jet expansion. The highly nonmonotonic quantum state dependent structure is all quite reproducible; experimental uncertainties are  $\approx 5\%$  of the reported values.

Intermediate $\text{H}_2\text{O}$ state vibration		$J_{K_a K_c}$	OH state	$N_{\text{OH}}$					
				1	2	3	4	5	6
$ 03^- \rangle$	$0_{00}$	$2\Pi_{3/2}^+$	31	4.4	2.0	1.0	0.2	0.2	
		$2\Pi_{1/2}^+$	10	2.2	2.4	1.3	0.3	0.5	
		$2\Pi_{3/2}^-$	4.9	26	4.5	3.1	4.3	0.3	
	$1_{01}$	$2\Pi_{3/2}^+$	9.4	15	2.5	1.0	0.4	0.0	
		$2\Pi_{1/2}^+$	3.4	7.7	2.2	1.4	0.40	0.2	
		$2\Pi_{3/2}^-$	21	12	14.5	5.2	2.5	1.8	
	$2_{02}$	$2\Pi_{3/2}^+$	5.1	15	4.2	0.9	0.6	0.1	
		$2\Pi_{1/2}^+$	2.1	8.4	2.9	1.3	0.9	0.1	
		$2\Pi_{3/2}^-$	23	9.8	14	7.1	1.8	2.2	
	$2_{20}$	$2\Pi_{3/2}^+$	16	4.2	12	2.9	0.4	0.3	
		$2\Pi_{1/2}^+$	6.0	2.7	9.8	2.9	0.6	0.9	
		$2\Pi_{3/2}^-$	5.3	18	7.2	5.9	3.8	0.4	
	$ 12^- \rangle$	$0_{00}$	$2\Pi_{3/2}^+$	29	2.4	3.6	0.6	1.1	1.0
			$2\Pi_{1/2}^+$	9.5	0.9	4.7	2.2	1.4	0.5
			$2\Pi_{3/2}^-$	2.5	23	2.1	9.4	3.5	1.8
$1_{01}$		$2\Pi_{3/2}^+$	16.9	9.7	3.0	1.7	0.7	0.8	
		$2\Pi_{1/2}^+$	5.3	5.9	3.0	2.5	0.8	1.0	
		$2\Pi_{3/2}^-$	12	15	5.9	7.1	5.3	2.1	
$2_{02}$		$2\Pi_{3/2}^+$	6.2	14	3.0	2.7	0.9	1.1	
		$2\Pi_{1/2}^+$	3.1	7.9	2.8	3.4	1.5	0.9	
		$2\Pi_{3/2}^-$	18	6.4	14.5	4.9	6.0	2.9	
$ 03^+ \rangle$	$1_{10}$	$2\Pi_{3/2}^+$	2.9	19	4.0	0.7	0.6	0.1	
		$2\Pi_{1/2}^+$	1.1	11	2.6	1.2	0.8	0.1	
		$2\Pi_{3/2}^-$	25	7.9	12	7.8	1.0	1.9	
	$1_{11}$	$2\Pi_{3/2}^+$	33	12	4.8	1.0	0.5	0.2	
		$2\Pi_{1/2}^+$	10.0	6.6	4.4	1.5	0.8	0.3	
		$2\Pi_{3/2}^-$	5.9	12	1.5	3.4	1.5	0.5	
	$2_{12}$	$2\Pi_{3/2}^+$	29	4.2	5.9	1.6	0.3	0.3	
		$2\Pi_{1/2}^+$	9.6	2.2	5.2	1.8	0.5	0.5	
		$2\Pi_{3/2}^-$	4.5	24	0.7	4.9	4.7	0.5	
$ 12^+ \rangle$	$1_{10}$	$2\Pi_{3/2}^+$	2.7	17	2.2	1.8	0.9	0.0	
		$2\Pi_{1/2}^+$	1.1	10	1.3	2.4	0.8	0.4	
		$2\Pi_{3/2}^-$	29	4.7	8.8	1.2	1.3	0.1	
	$2_{12}$	$2\Pi_{3/2}^+$	22	4.7	8.8	1.2	1.3	0.1	
		$2\Pi_{1/2}^+$	7.0	1.6	6.3	1.5	1.1	0.3	
		$2\Pi_{3/2}^-$	4.3	22	1.8	10	3.1	1.8	

$0_{00}$ . However, as also demonstrated in Fig. 9, strong qualitative differences are observed for some initial rotational levels such as  $1_{01}$ , where the phase of the OH lambda doublet oscillations clearly reverses between  $|12^- \rangle$  versus  $|03^- \rangle$  states. Due to the finite number of levels sampled in the slit jet, it is not clear if this effect is isolated to one or a few rotational states, or whether similar discrepancies would also be evident in higher rotational states. Nevertheless the data in Fig. 9 indicate that quite different dynamical behavior can be observed even for states of the *same* total angular momentum.

It is worth noting that a strong dependence of OH product distributions on initial vibrational state for a given intermediate rotational level has been also observed in the  $v_{\text{OH}}=4$  and 5 manifold by Brouard, Langford, and Manolopoulos.<sup>7</sup> Specifically, photolysis of  $J_{K_a K_c}=4_{04}$   $\text{H}_2\text{O}$  results in dramatically different OH rotational distributions depending on whether the intermediate vibrational level is  $|04^- \rangle$  and  $|05^- \rangle$ . Similar to the present work, these studies were performed at total energies that sampled initial  $\text{H}_2\text{O}$  vibrational states localized far out into the exit channel.

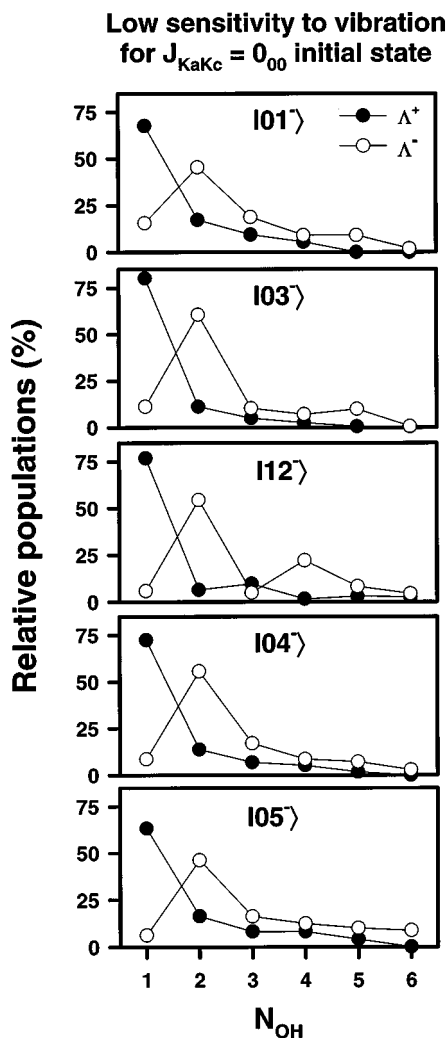


FIG. 8. OH rotational product state distributions obtained from photolysis of H<sub>2</sub>O in the same 0<sub>00</sub> rotational state, but for a range of initial vibrational states. Data for the |01<sup>-</sup>⟩, |04<sup>-</sup>⟩, and |05<sup>-</sup>⟩ states come from Refs. 3, 10, and 7, respectively. Note the remarkable insensitivity to initial vibrational state and how well the current  $\nu_{\text{OH}}=3$  data for 0<sub>00</sub> support the trend.

These behaviors have been rationalized by Brouard, Langford, and Manolopoulos<sup>7</sup> in a physically plausible modification of the Franck–Condon model by allowing the OH bond lengths to vary with initial vibrational level. Interestingly, they find that by fixing the OH spectator bond and varying the fragmenting Jacobi coordinate H–OH bond length from values corresponding to the ground state equilibrium separation to values corresponding to a vibrationally “pre-stretched” OH bond brings the theoretical predictions into better agreement with the experiment. Indeed, much of the oscillatory rotational state dependent trends in the  $\nu_{\text{OH}}=4$  and 5 data could be qualitatively reproduced by shifting the Jacobi coordinate over a relatively small window of  $\Delta R \approx 0.25 \text{ \AA}$ .

There are two contributions to this effect in the context of the modified rotational Franck–Condon model. First, the rotational constants of the rigid bender/rotor change as the initial Jacobi H–OH bond length is increased. Second, for different values of  $R$ , a rigid bender model samples a different part of the intramolecular PES, which therefore changes

### OH rotational distributions, H<sub>2</sub>O J=1 states

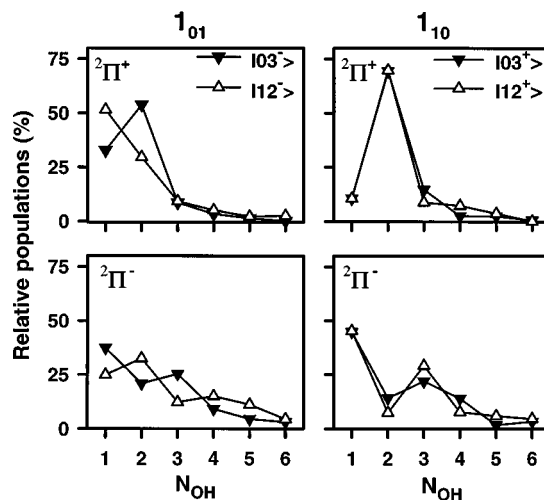


FIG. 9. OH product rotational distributions for photodissociation of 1<sub>01</sub> and 1<sub>10</sub> states of H<sub>2</sub>O from all four intermediate vibrational states. The filled circles represent the data from |03<sup>-</sup>⟩ and |03<sup>+</sup>⟩ initial H<sub>2</sub>O vibration, while the unfilled circles represent data for |12<sup>-</sup>⟩ and |12<sup>+</sup>⟩ vibrations. For the 1<sub>01</sub> rotational state, there are quite significant differences in distributions originating from |03<sup>-</sup>⟩ and |12<sup>-</sup>⟩ initial vibrational states, respectively.

the effective 1D potential used to calculate the bending wave functions. As mentioned above, it has been argued<sup>7</sup> that contributions from those two effects may fortuitously cancel for the 0<sub>00</sub> state of H<sub>2</sub>O, but that this balance could be upset in higher rotational states. This would suggest that sensitivity in the photofragment distributions to initial vibrational state would show some systematic increase with rotational excitation. However, the current  $\nu_{\text{OH}}=3$  overtone data tend not to support this hypothesis, since, for example, much bigger initial vibrational state sensitivities are observed in the 1<sub>01</sub> state, than in, for example, either of the 2<sub>02</sub> and 2<sub>12</sub> states.

As a final note, we have attempted to model these product state distributions for the 1<sub>01</sub> state in the context of the modified rotational Franck–Condon model by changing the Jacobi H–OH bond length (see Fig. 10). It would appear that the modified Franck–Condon model is generally in better agreement with the |03<sup>-</sup>⟩ data for increased values of  $R$ . However, even for  $\Delta R$  up to 0.4 Å (i.e., the upper limit of what might be physically justified for  $\nu_{\text{OH}}=3$  excitation), the Franck–Condon model is not able to reproduce the experimentally observed distributions for |12<sup>-</sup>⟩. Such anomalous photolysis behavior for isolated rovibrational states again suggests the importance of specific resonances in the exit channel between stretching, bending, and overall rotational degrees of freedom, and therefore a much richer and more complicated range of photofragmentation dynamics than can be currently predicted by Franck–Condon models.

### V. SUMMARY

The photodissociation of state-selected H<sub>2</sub>O has been studied in the second OH stretch overtone manifold by vibrationally mediated photolysis techniques at 248 nm. By choice of far off resonance photolysis wavelength and low

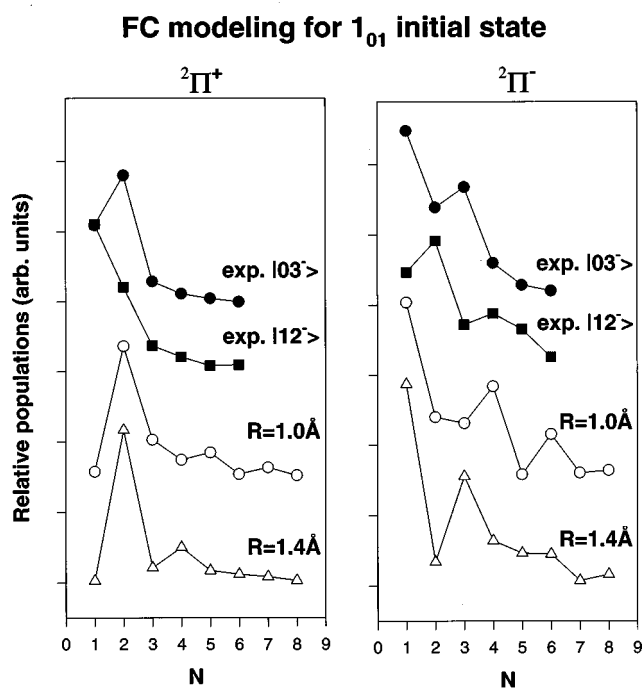


FIG. 10. Comparison of experimental OH distributions (filled symbols) with the predictions of the rotational Franck–Condon model (open symbols), with the results offset along the vertical axis for purposes of clarity. The spectator OH bond length is held fixed at  $r = 1.0 \text{ \AA}$ , while the initial H–OH Jacobi coordinate has been adjusted by  $\Delta R \approx 0.4 \text{ \AA}$  between  $R = 1.0 \text{ \AA}$  and  $R = 1.4 \text{ \AA}$  without qualitatively reproducing the experimentally observed differences.

total excess energies, Franck–Condon dissociation from the  $\nu_{\text{OH}} = 3$  manifold occurs via excitation significantly into the exit channel on the upper potential surface. This has a significant effect on OH product vibrational distributions; specifically, only the  $\nu_{\text{OH}} = 0$  product is observed for both the  $|12^- \rangle$  and  $|03^- \rangle$  initial vibrational states, with an upper limit on the ratio of  $\text{OH}(\nu = 1)/\text{OH}(\nu = 0)$  of  $< 1\% - 2\%$ . This is in contrast to previous vibrationally mediated photolysis studies in the  $\nu_{\text{OH}} = 4$  manifold at higher total excess energies accessing the Franck–Condon region, for which local mode pre-excitation in the spectator OH bond was found to be adiabatically conserved in the photolysis event.

Relative UV photodissociation cross sections out of the  $|03^+ \rangle$ ,  $|03^- \rangle$ ,  $|12^+ \rangle$ , and  $|12^- \rangle$  manifold of states are extracted by integrating over all final OH distributions and normalizing to relative IR cross sections, laser power, etc. in the overtone excitation step. Though not evident in the OH vibrational state distributions, the selectivity to initial  $\text{H}_2\text{O}$  vibrational state is extremely high, for example, with more than an order of magnitude differences observed between photolysis cross sections for  $|03^- \rangle$  and  $|12^- \rangle$  levels. The results have been theoretically interpreted in terms of Franck–Condon overlap between the vibrational wave functions for  $\text{H}_2\text{O}$  on the ground state surface, the transition dipole surface for electronic excitation, and the continuum wave functions for  $\text{H} + \text{OH}$  on the excited state potential surface. 2D quantum calculations of these dipole transition matrix elements yield results in qualitatively good agreement with these experimental observations.

Rotational,  $\Lambda$ -doublet and spin-orbit state distributions of the OH product have been obtained for the complete set of initial rotational states accessible via dipole excitation from jet-cooled  $0_{00}$  and  $1_{01}$   $\text{H}_2\text{O}$ . In agreement with previous studies<sup>3,10,12</sup> in other overtone manifolds, the results support a general insensitivity of the product rotational distributions to the initial vibration excited. This effect is most clearly demonstrated for photodissociation out of the lowest  $\text{H}_2\text{O}$  rotational state  $0_{00}$ , where the rotational distributions are nearly identical for levels of OH stretch excitation ranging from  $\nu_{\text{OH}} = 1$  to 5 quanta. This is in good qualitative agreement with Franck–Condon model of Balint-Kurti and co-workers, which predicts final state distributions from projecting the initial  $\text{H}_2\text{O}$  rigid bender wave function onto a complete set of final OH rotor states. However, deviations from this general trend are clearly observed for specific initial  $J > 0$  rotational states of  $\text{H}_2\text{O}$ . This sensitivity to OH stretch-vibrational state is not consistent with predictions of the rotational Franck–Condon model, nor can the data be accounted for by simple modifications of this model that include pre-extension of the OH bond to be broken. This complex photolysis behavior is likely to require more refined models of the dissociation event, which, for example, include exit channel interactions between stretching, bending and overall molecular rotation in the outgoing products.

## ACKNOWLEDGMENTS

This work has been supported by grants from the National Science Foundation. The authors would like to thank to Professor Mark Brouard and Dr. Stephen Langford for graciously providing us with the computer codes for rotational Franck–Condon calculations and for many stimulating discussions.

- <sup>1</sup>J. R. Huber and R. Schinke, *J. Phys. Chem.* **97**, 3463 (1993).
- <sup>2</sup>R. N. Dixon, *Chem. Soc. Rev.* **23**, 375 (1994).
- <sup>3</sup>D. Hausler, P. Andresen, and R. Schinke, *J. Chem. Phys.* **87**, 3949 (1987).
- <sup>4</sup>P. Andresen, G. S. Ondrey, B. Titze, and E. W. Rothe, *J. Chem. Phys.* **80**, 2548 (1984).
- <sup>5</sup>I. Bar, D. David, and S. Rosenwaks, *Chem. Phys.* **187**, 21 (1994).
- <sup>6</sup>M. Brouard and S. R. Langford, *J. Chem. Phys.* **106**, 6354 (1997).
- <sup>7</sup>M. Brouard, S. R. Langford, and D. E. Manolopoulos, *J. Chem. Phys.* **101**, 7458 (1994).
- <sup>8</sup>D. David, A. Strugano, I. Bar, and S. Rosenwaks, *J. Chem. Phys.* **98**, 409 (1993).
- <sup>9</sup>R. L. Vander Wal, J. L. Scott, and F. F. Crim, *J. Chem. Phys.* **94**, 3548 (1991).
- <sup>10</sup>R. L. Vander Wal, J. L. Scott, and F. F. Crim, *J. Chem. Phys.* **94**, 1859 (1991).
- <sup>11</sup>R. Schinke, R. L. Vander Wal, J. L. Scott, and F. F. Crim, *J. Chem. Phys.* **94**, 283 (1991).
- <sup>12</sup>V. Engel, V. Staemmler, R. L. Vander Wal, F. F. Crim, R. J. Sension, B. Hudson, P. Andresen, S. Hennig, K. Weide, and R. Schinke, *J. Phys. Chem.* **96**, 3201 (1992).
- <sup>13</sup>H. T. Wang, W. S. Felps, and S. P. McGlynn, *J. Chem. Phys.* **67**, 2614 (1977).
- <sup>14</sup>W. L. Dimpfl and J. L. Kinsey, *J. Quant. Spectrosc. Radiat. Transf.* **21**, 233 (1979).
- <sup>15</sup>G. H. Dieke and H. M. Crosswhite, *J. Quant. Spectrosc. Radiat. Transf.* **2**, 97 (1962).
- <sup>16</sup>V. Staemmler and A. Palma, *Chem. Phys.* **93**, 63 (1985).
- <sup>17</sup>R. Schinke, V. Engel, and V. Staemmler, *Chem. Phys. Lett.* **116**, 165 (1985).
- <sup>18</sup>R. Schinke, V. Engel, and V. Staemmler, *J. Chem. Phys.* **83**, 4522 (1985).

- <sup>19</sup>V. Engel, R. Schinke, and V. Staemmler, *J. Chem. Phys.* **88**, 129 (1988).
- <sup>20</sup>J. Zhang and D. G. Imre, *J. Chem. Phys.* **90**, 1666 (1989).
- <sup>21</sup>K. Weide, S. Hennig, and R. Schinke, *J. Chem. Phys.* **91**, 7630 (1989).
- <sup>22</sup>M. V. Dirke and R. Schinke, *Chem. Phys. Lett.* **196**, 51 (1992).
- <sup>23</sup>G. G. Balint-Kurti, *J. Chem. Phys.* **84**, 4443 (1985).
- <sup>24</sup>D. F. Plusquellic, O. Votava, and D. J. Nesbitt, *J. Chem. Phys.* **107**, 6123 (1997).
- <sup>25</sup>O. Votava, J. R. Fair, David F. Plusquellic, E. Riedle, and D. J. Nesbitt, *J. Chem. Phys.* **107**, 8854 (1997).
- <sup>26</sup>D. F. Plusquellic, O. Votava, and D. J. Nesbitt, *Appl. Opt.* **35**, 1464 (1996).
- <sup>27</sup>L. S. Rothman, HITRAN database (ONTAR, 1996).
- <sup>28</sup>K. S. Sorbie and J. N. Murrell, *Mol. Phys.* **29**, 1387 (1975).
- <sup>29</sup>M. S. Child, *Semiclassical Mechanics with Molecular Applications*, 1st ed. (Oxford University Press, New York, 1991).